Materials & Design 233 (2023) 112187

Contents lists available at ScienceDirect

Materials & Design

journal homepage: www.elsevier.com/locate/matdes

FIB-SEM investigation and uniaxial compression of flexible graphite

E. Solfiti [a,*], D. Wan [a,**], A. Celotto [a], N. Solieri [c], P.A. Muñoz [c], R.F. Ximenes [c], J.M. Heredia [c], C.L. Torregrosa Martin [c], A. Perillo-Marcone [c], F.X. Nuiry [c], A. Alvaro [b], F. Berto [a,d], M. Calviani [c]

[a] Department of Mechanical and Industrial Engineering, Norwegian University of Science and Technology, Richard Birkelands vei 2B, Trondheim, 7491, Norway
[b] Department of Material and Nanotechnology, SINTEF Industry, Richard Birkelands vei 3, Trondheim, 7034, Norway
[c] CERN, Geneva, Switzerland
[d] Department of Chemical Engineering, Sapienza University of Rome, Rome, Italy

ARTICLE INFO

Keywords:
Flexible graphite
FIB-SEM
Uniaxial compression

ABSTRACT

Flexible graphite (FG) with $\rho = 1$ g/cm^3 density is a type of highly porous and anisotropic graphite, mainly used for gaskets and sealing applications, but also suitable for energy absorption, such as in the beam dumping devices of the Large Hadron Collider (see Heredia 2021 [1]). Knowledge of its microstructure and mechanical properties needs to be developed for the selection of an adequate material model able accurately predict stresses and failure in FG components. Here, the FG microstructure properties available in literature are reviewed, followed by Focused Ion Beam - Scanning Electron Microscopy investigation and compression tests. Specifically, a single 100 μm × 150 μm cross section was obtained, and the 2D pore sizes and shapes were quantified using image segmentation. Monotonic and cyclic out-of-plane compression tests were performed in single and stacked configuration. Stress-strain curves showed three domains: the initial toe, the transition and the densification domain. The cyclic tangent modulus was also calculated from the cyclic tests. Many observations suggested that FG behaves similarly to crushable foams, crumpled materials and compacted powders, and that both crystalline microstructure and crumpled mesostructure play a predominant role in the deformation mechanism.

1. Introduction

Flexible graphite (FG) is obtained by uniaxial or rolling compression of expanded graphite particles without any additive binder [2], unlike polycrystalline and pyrolytic graphite. Due to its high porosity and particular microstructure, FG shows good conformability, resilience and viscous properties that make it particularly suitable for sealing and gasket applications [3], often in sandwiched structures with stainless steel foils [4] or in the shape of tapes and impregnated yarns [5]. Other applications that exploit the remarkable thermal conductivity and chemical resistance are heat exchange devices for microelectronics [6,7], thermal interfaces [8], electromagnetic field shielding [9], resistive heating elements [10], fuel cell proton exchange membranes [11], electrochemical electrodes for batteries [12] and stress sensing devices [13]. In addition to this diversified list, a further implementation of FG is the Target Dump External (TDE) block (Fig. 1) responsible for the energy absorption of the proton beam extracted from the Large Hadron Collider (LHC) [1]. The latter is considered as the world's largest and most powerful particle accelerator [14] and is located in Geneva (Switzerland) at the facilities of the European Organization for Nuclear Research (CERN). Its purpose is to reveal the physics beyond the Standard Model with collisions of proton beams reaching up to 14 TeV centre of mass energy [15]. The TDE block is part of the LHC Beam Dump System, a critical section for the safety of LHC operations [16], and consists in a 318LN stainless steel cylindrical vessel (length = 8500 mm, external diameter = 712 mm, thickness = 12 mm) containing a series of graphitic materials that includes: 6 isostatic polycrystalline graphite blocks (SGL Sigrafine® 7300 [5]), 700 mm long and with a density $\rho = 1.73$ g/cm^3; a low-density section with 1650 FG sheets (SGL Sigraflex® L20012C [5]), 2 mm thick and $\rho = 1.2$ g/cm^3, stacked together and supported at the ends by two SGL Sigrafine® HLM [5] plates (80 mm thick and $\rho = 1.72$ g/cm^3); two titanium-alloy windows that enclose the whole vessel. The apparatus is filled with nitrogen gas and the beam is swept in a pseudo-elliptical spiral path that optimizes the energy deposition

* Corresponding author.
** Current affiliation: Advanced Research Institute of Multidisciplinary Sciences, Beijing Institute of Technology, Zhongguancun South Street 5, 100081 Beijing, China.
E-mail address: emanuele.solfiti@ntnu.no (E. Solfiti).

https://doi.org/10.1016/j.matdes.2023.112187
Received 6 January 2023; Received in revised form 20 July 2023; Accepted 20 July 2023
Available online 26 July 2023

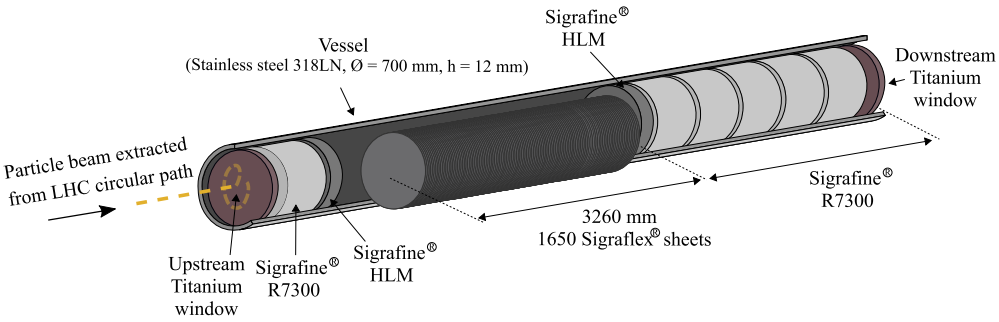

Fig. 1. Schematic illustration of the Target Dump External (TDE) block.

over the material volume [16]. The choice of graphite-based materials is dictated by their high performances in terms of beam absorption, as they show a good combination of thermophysical properties, especially low density and low specific heat, to minimise the temperature increase during beam impact [17]. Among the different materials, the Sigraflex® section is designed to be the most exposed with temperatures up to 1500 °C and 2300 °C under nominal and worst-case scenario conditions, respectively [1]. Besides the thermal load, the sudden expansion of the heated volume results in a multi-axial dynamic stress state that requires coupled thermal and mechanical analysis to be reliably predicted; the accuracy of such predictions, usually obtained by finite element simulations [18], is based on accurate constitutive models of the materials involved. However, only a very few proposals of FG modeling were presented in previous investigations [4,19,20] and the information is not sufficient to select or formulate a constitutive model suitable for Sigraflex® or FG with similar density. This work therefore represents a basic step in developing such a model, starting from a deep microstructure investigation and from the observation of the out-of-plane compression response at room temperature.

Relevant information on microstructure and mechanical properties available in the literature is first reported, followed by a Focused Ion Beam - Scanning Electron Microscope (FIB-SEM) investigation and out-of-plane compression tests. FIB-SEM has already been applied to different types of graphite and carbon-based materials [21] and proved effective for the reconstruction of microstructures with complex pore space [22]. Advanced image-segmentation techniques are usually employed to transform the images into an image-based model [23] used either for quantification of characteristic pore size and distribution [24] or to predict mechanical properties [25]. However, to the authors' knowledge, FIB-SEM has never been applied to FG, and although SEM images of fractured sections have been obtained in previous works [6,26,27], extraction of quantitative properties from images has never been attempted. Here, the morphology of pores and carbon microsheets is shown, and the characteristic 2D pore sizes are extracted by a segmentation algorithm optimized on a single FIB-milled section. The goal includes the assessment of FIB-SEM and image segmentation capabilities on capturing FG microstructure for future extension to 3D tomography, microstructure reconstruction and micromechanical modeling. The latter aims not only to the prediction of FG structural response, but also to the analysis of pore-fluids interaction, fundamental in most of FG applications such as electrodes and plates for batteries [13].

The out-of-plane compression test has been already used in previous works to calibrate a hyper-elastic Blatz-Ko foam constitutive law for spiral-wound FG gaskets simulation [4,20]. Loading-unloading stress-strain curves have also been obtained in other works [26,28], but without any related analytical or numerical modeling proposal. In this work, the main mechanical properties, such as the yield strength and the tangent modulus, are discussed, as well as the similarities of the stress-strain curves with other known materials such as crumpled materials. The latter are obtained by crumpling of thin sheets usually made of paper [29], aluminum [30,31] and graphene [32,33]. Although crumpled materials show several similarities with foams and entangled fibrous materials [29], they are easier and cheaper to produce [34], and their properties originate from the structure rather than the composition of the material [35]. The pores indeed are not inclusions of a continuous matrix but reside in between irreversible folds that interact by contact forces and constitute what is referred to here as *mesostructure*. Regardless of such a complex porous structure, their mechanical properties are well-reproducible and can be exploited in engineering applications such as alternative to standard polymer foams [29], for energy absorption in core of sandwich panels [36] or for creating meta-biomaterials to treat segmental bone defects [37]. Interest on crumpled materials has also increased in recent years due to the design of new materials with unique and adjustable properties not normally found in nature [35,38]. Similarities on the compression behavior of FG and crumpled materials are highlighted in the following.

The outcomes are believed to constitute a first step toward the development of a constitutive model for FG: this is not only necessary for the TDE modeling, but can substantially improve the mechanical performances of other FG applications such as sealing, gaskets and electrodes. However, the analysis is limited to the only mechanical out-of-plane response, and does not take into account multiaxial stress states as well as the coupling of behaviors in different directions is not attempted.

2. FG microstructure and mechanical properties

A summary of a general FG production process is given in Fig. 2. The raw material used is natural graphite, i.e. a purely crystalline ore material having the form of flakes and plates whose thickness and diameter are in the order of magnitude of 10^1 μm and 10^2 μm, respectively [39]. Sulfuric and nitric acids are chosen to penetrate among the basal planes during the intercalation phase, and rapid heating is applied to obtain the exfoliated powder. The smaller the thickness-to-diameter ratio of the flakes, the larger the resulting expanded volume [40]. The expanded particles are commonly referred to as *worms* due to their accordion-like shape and, thanks to their jagged profile, can be compressed together to create compacts or sheets with tailored density and thickness. Typically, materials denser than 0.7 - 0.8 g/cm^3 and up to 1.8 – 1.9 g/cm^3 are referred to as FG whereas materials with lower density are simply called graphite compacts or compressed expanded graphite. It is basically impossible to obtain density higher than 1.8 – 1.9 g/cm^3 due to the difficulty on applying further irreversible work of compression [6,26]. For the sake of clarity, the following nomenclature will be adopted throughout the text (see Fig. 2):

- Natural graphite flakes: raw material made of purely crystalline graphite flakes,
- Worms or exfoliated graphite: flakes after expansion. They have large pores, also called cells, and their
- microsheets: stacks of tens of carbon basal planes. The skeletal structure of each single worm is a stack of corrugated microsheets. Cell walls and microsheets refer essentially to the same entities, except that the first term is more appropriate when referring to exfoliated graphite.

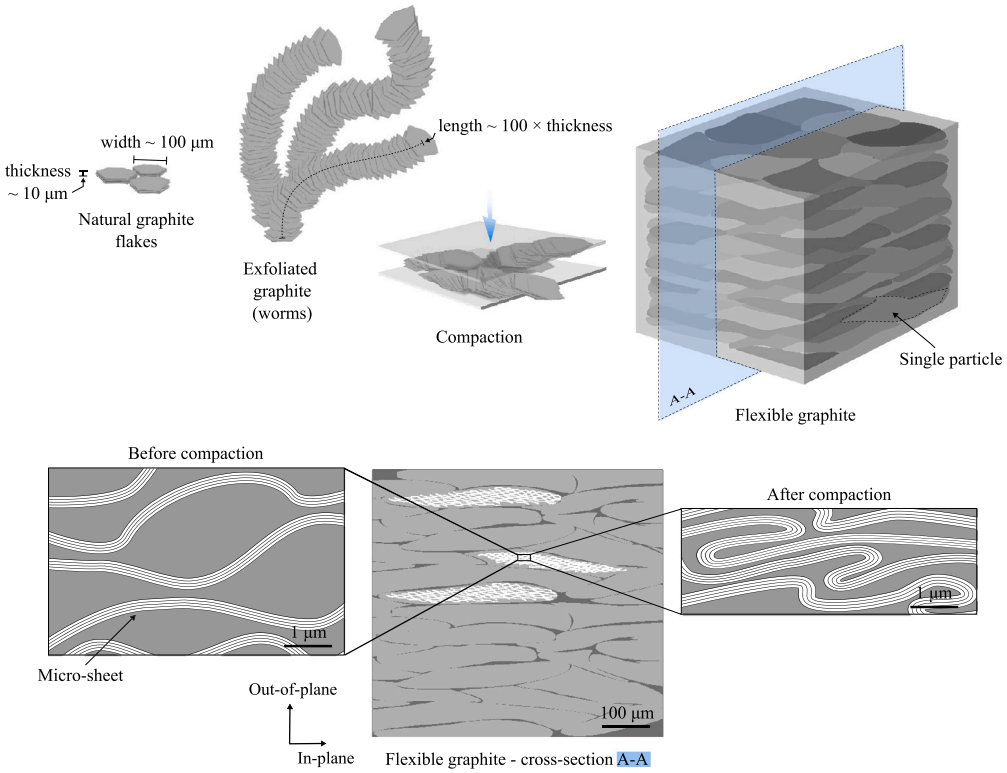

Fig. 2. Top: production process of FG. The compaction stage is usually made by rolling compression up to $\rho = 0.7 - 1.9$ g/cm^3. Bottom: expected deformation mode of worm cells under compression.

- Particles: worms intended as entities inside the compacted materials. They are mainly flattened along the bedding plane,
- Out-of-plane and in-plane directions: perpendicular and parallel to the bedding plane, respectively,
- Compaction: the compression stage of the production process.

Thus, in general, a bottom-up hierarchical system can be identified at different length scales of FG microstructure: the carbon basal planes (nm) inside the microsheets (μm), the microsheets inside the particles (10 - 100 μm) and the interlocked particles as structural units of the bulk material (mm).

The uncompressed worms have densities around 0.004 - 0.015 g/cm^3 (porosity $P > 99\%$) [41,42] and their morphology depends on the size of initial flakes [43,44], as well as on production process parameters such as expansion temperature [40] and intercalating species [45]. Their final length can reach up to 100 - 300 times the initial thickness, whereas the width corresponds to the original width of the particles, on the order of 100 μm.

Irregular honeycomb-shaped cells are randomly dispersed along the body of the worms as a result of the expansion of the intercallants [41]. The characteristic size of the single cell (wall-to-wall) was measured by SEM imaging in worms of three different densities, namely 0.006 g/cm^3, 0.009-0.011 g/cm^3 and 0.004 g/cm^3: these were found to have ellipsoidal shapes with major axis between 21 to 32 μm and the minor axis between 10 to 16 μm [42]. Pore sizes as large as 100 – 200 μm were also reported in the plotted distribution. The average aspect ratio was about 0.5. The Johnson, Koplik and Schwartz (JKS) describe reasonably well the pores by assuming cylindrical shapes with equal lengths and diameters [41], and was used to infer that the pore sizes decrease from 1.36 μm to 0.078 μm as the densities compacts increase from 0.0236 g/cm^3 to 0.35 g/cm^3 [46]. The anisotropy and tortuosity of the pore network increases with the density, which can be related to the permeability and formation factor by simple power laws [47].

Cell wall thickness, as calculated by nitrogen adsorption and specific surface area, was found to be equivalent to 48 – 68 basal planes, or equivalently 16 – 22 nm [41,48]. A higher estimate for the wall thickness, corresponding to 30 – 60 nm, was provided in a previous SEM imaging analysis [26].

During the compaction, the cell walls are severely crumpled and tend to be aligned, together with their inner carbon basal planes, along the in-plane direction. Their average orientation with respect to this direction at $\rho = 1$ g/cm^3 was found to be between 9° and 15° [6]. In low-density compacts, it was observed that the relative displacement of adjacent basal planes within the cell wall is relatively small, and the main contribution to the large deformation is given by the relative displacement between adjacent walls [43,46,48]. The overall deformation of a worm is governed by its bending and thickness reduction [49] while jagged boundaries are responsible for creating interlocking forces between neighboring worms as they become flat particles. Although strongly agglomerated, the single particles, or clusters of particles, seem to retain their identity inside the final sheet. Indeed, in presence of tensile forces along the in-plane direction, the fracture propagates mainly along the particle boundaries [27], whereas, in presence of out-of-plane forces, the deformation field evolves homogeneously within rod- and sheet-shaped volumes with average maximum diameters between 100 and 150 μm, referred to as *deformation units* [50].

The number of links between particles increases in proportion to density, and their effectiveness is ascribed to the initial relative misalignment between adjacent microsheets [26]. In general, larger is the initial flake size, larger the exfoliated volume and better the mutual folding between the microsheets. The effectiveness of particles cohesion governs the in-plane tensile strength [44,51] while the elastic modulus results from unwrinkling of microsheets [26]. The presence of two types of microstructural region was suggested by SEM imaging and X-ray diffraction: the first type has well-aligned basal planes and slightly misaligned microsheetswhile the second is stiffer and has highly wrinkled microsheets. The elastic response in out-of-plane compression was attributed mainly to the deformation of aligned regions while the misaligned regions were responsible for the unrecovered deformation [26].

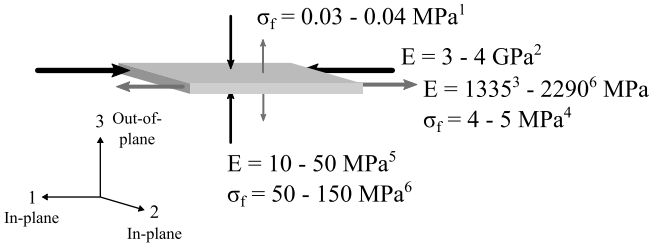

Fig. 3. Visual summary of elastic moduli and yield strengths for 1 g/cm^3 FG. In-plane isotropy is assumed. [1]Data from [27], [2]Data from [53], [3]Data from [13], [4]Data from [56], [5]Data from [28], [6]Data from [26].

Porosity at the end of compaction results from inter- and intra-particle contributions: the bulk density and the particle density have been linearly correlated so that, for example, when the bulk density reaches 1 g/cm^3, each particle is compressed from 0.015 g/cm^3 up to 1.2 – 1.8 g/cm^3 [41]. Visual access is made difficult by the ease of delamination of the material [6], so non-destructive techniques such as mercury porosimetry and nitrogen adsorption-desorption are usually needed for porosity characterization. These revealed the presence of three different size categories at ρ = 1 g/cm^3: macro-pores (> 40 nm), meso-pores (< 40 nm, characteristic size between 1.5 and 6 nm) and micro-pores (inter-crystalline cavities) [40,52]. The pore shape can probably be approximated by disks oriented mainly along the in-plane direction [53], with a resulting permeability in this direction about 2-3 times higher than in the out-of-plane direction.

The amount of open or closed porosity at 1 g/cm^3 is still to be clarified: a percentage of 30% closed porosity was found at ρ = 0.14 g/cm^3 [41], while only 8% was deduced from the rule of mixture of homogeneously distributed closed and open pores in FG with 1 g/cm^3 [49]. Further observations implies that: if the total volume occupied by both meso- and macro-pores in 1 g/cm^3 FG specimens was 0.51 – 0.59 cm^3/g [40], as well as the porosity was 0.51 – 0.59 for 1 g/cm^3 samples, and if the theoretical porosity is calculated as $P = 1 - \rho_0/\rho_s = 0.56$, where ρ_0 = 1 g/cm^3 and ρ_s = 2.26 g/cm^3 is the density of crystalline graphite [54], then the uncertainty of the measurements precludes a good estimation of the open porosity, which cannot exceed 9% in any case.

From a macroscopical point of view, a FG foil with ρ = 0.7 - 1.9 g/cm^3 appears as a relatively soft, flexible and inelastic material. It can be easily delaminated by low bending forces applied in the in-plane direction, and obvious slip planes can be distinguished in the deformed regions. Transversal isotropy is usually assumed in the in-plane directions, but large difference can be found in strength and elastic modulus between the in-plane and out-of-plane directions. A visual summary of FG material properties is shown in Fig. 3 obtained from previously reviewed literature [39,55]. The low-loads stress-strain response (maximum load = 1 MPa and maximum engineering strain less than 6%) of FG at different densities i.e., 0.55, 1.05, 1.54, 1.7 g/cm^3, showed full elastic recovery with non-linear behavior and little hysteresis [28]. While the curves at higher loads were similar to crushable foams or granular powders [20], the low-loads behavior reported appears inconsistent for these materials and needs to be further investigated.

3. Method

3.1. FIB-SEM investigation

This analysis was carried out on 1 g/cm^3 Sigraflex® with 2 mm thickness and 2% ash content [5]. A transversal cross-section of a specimen free from any processing marks was cut by employing a Ga$^+$ FIB-SEM microscope (FEI Helios G4-UX). The sample surface was first prepared by platinum deposition along the top edge of the desired section. This was meant to be sacrificial for the cross-sectioning while limiting the tail and curtaining effects by leveling the superficial asperities. Then, the cross-section was milled by ion sputtering (30 kV, 65 nA) along parallel stripes, at increasing depth, from the surface down to approximately 100 μm. An ion current of 2.8 nA was adopted in the last milling step to finely smooth the surface. The final section was rectangular with sides of 100 μm × 150 μm, perpendicular to the slicing direction as in Fig. 4.

Table 1
Number of tests per each loading case.

	Monotonic	Cyclic
Single specimens	8	17
Six-unit specimens	4	1

The SEM images were acquired in secondary electron mode and adjusted to a perpendicular view. The segmentation procedure was carried out in MATLAB® using Image processing Toolbox^{TM} and was based on marker-controlled watershed transform and two-dimensional Fourier transform filtering (further details can be found in Appendix A). Four parameters were chosen to describe the pore morphology i.e., the equivalent radius $R_{eq} = \sqrt{Area/\pi}$, the radius of the maximum inscribed circles R_{ins} taken as the maximum of the distance transform per each pore, the maximum radius R_{max} taken as half of the maximum Feret diameter, and the aspect ratio $AR = R_{ins}/R_{max}$. Their probability distribution were fitted by a log-normal distribution function, as shown in Appendix B, and the numerical values of the μ, $\bar{\sigma}$ and the expected value were reported. The expected value of R_{eq} is commonly considered as the characteristic pore size. The porosity and the pore areas were calculated as the sum of pore pixels, converted to μm by pixel proportion. Since pores with area lower than 10 pixels were not included in the analysis, the pores under investigation are the only macro-pores, defined in a previous work [40], with characteristic size larger than 40 nm.

Finally, some particles were pulled apart from the specimen surface by the simple “scotch tape” technique (often used for graphitic materials to induce exfoliation [57]). The results did not add particular information to the study and, for completeness, are given in Appendix C.

3.2. Out-of-plane compression

Static and cyclic uniaxial compression tests were carried out using the same material described in section 3.1. The foils were hole punched in circular specimens with a nominal diameter of 26 mm, and tested by an Instron Electropuls® E10000 machine (maximum load ± 10 kN, load cell resolution ± 0.5 N) equipped with compression plates (Fig. 5a, top). In total, 25 tests were performed on single unit specimens and 5 tests on six-units stacked configuration (Fig. 5a, bottom). The number of specimen per each testing case is reported in Table 1. Recommendations from ASTM D695 [58] and ISO 13314 [59] were followed when possible. All the monotonic and cyclic displacements were applied at 0.1 mm/min rate by means of single or repeated triangular waveforms where, in some cases, a 30 seconds holding time was applied at the maxima and minima displacement peaks. One test was run at 0.01 mm/min and one in load control at 20 kPa/s (approximately equivalent to 0.1 mm/min displacement rate). In all tests, a preload of ≈ 0.03 MPa (≈ 15 N) was imposed to ensure contact between the plates and the specimen. In 7 cyclic tests, cyclic loading up to 1 MPa with a loading rate of 30-40 kPa/s was imposed for 6-10 cycles prior the actual test until satisfactory repeatability was observed in the load-unload curves. All the curves were plotted using the definition of true strain for compression:

$$\varepsilon = \ln \frac{h_0}{h}, \tag{1}$$

where h_0 = 2 mm is the initial (nominal) thickness and h is the current thickness. The engineering and true stresses σ were considered equal because of the small variation in the resistant area.

The tangent slope of the monotonic curve was estimated by the central difference method to define the transition between different domains, while the initial cyclic tangent modulus H of the cyclic response

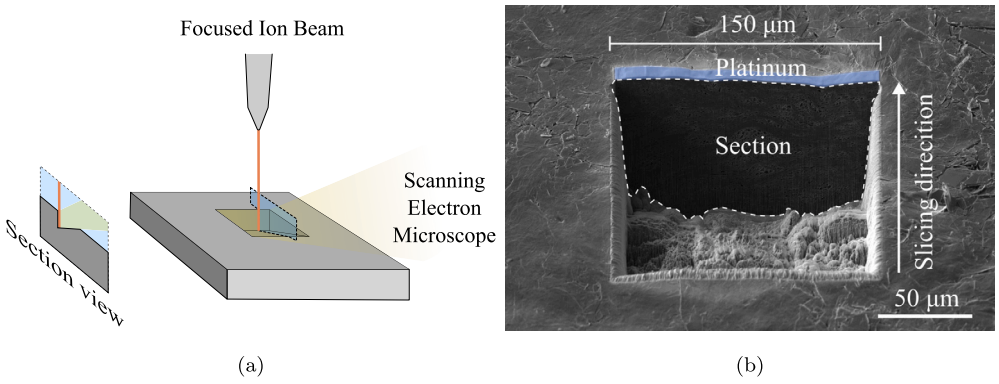

Fig. 4. (a) Schematic illustration of the section obtained by FIB-SEM and (b) top view of the actual section.

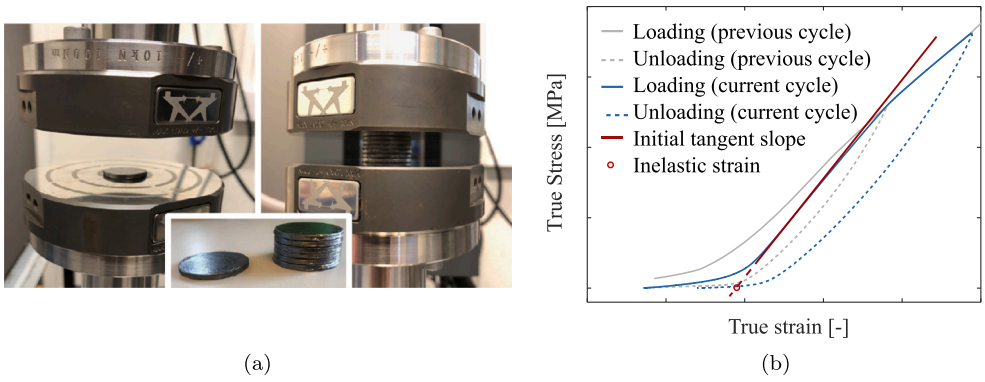

Fig. 5. (a) Geometry and test setup for single-sheet and stacked FG specimens, (b) initial cyclic tangent slope H and final inelastic strain definition.

was calculated to monitor the change in stiffness under increasing compressive loads. The calculation of the last quantity slightly differs from that of the elastic gradient used to characterize foams of various nature [59,60], but it is considered here as more meaningful because of the different FG production process. Due to the irregular shape of the hysteresis loops, the modulus was calculated per each cycle as the slope of the initial part of the loading path after the toe (Fig. 5b) and the cycles not reaching at least a peak stress of 0.5 MPa were not included in the calculation. The tangent line was extended downwards until it intersected the strain axis at ε_p which was considered to be the inelastic component of the total strain and used to define the final relative density ρ_p^* as

$$\rho_p^* = \frac{\rho_0}{\rho_s} e^{\varepsilon_p} \tag{2}$$

where $\rho_0 = 1$ g/cm^3, $\rho_s = 2.26$ g/cm^3, and no lateral deformation is assumed. This last hypothesis will be better argued *a posteriori* in section 4.2. Finally, the diameters and thicknesses of the specimens were measured with a digital calliper (± 0.01 mm resolution), at 5 random positions along the lateral and base surfaces before and after each test (at least 30 minutes later), so that the residual strains could be assessed in these directions.

4. Results

4.1. FIB-SEM investigation

Despite the curtain effect due to the high porosity, the microstructure obtained by FIB-SEM is considerably more obvious than in tension-fractured specimens images, such as those ones reported in literature [6] or on the right side of Fig. 6. Two types of regions can be identified visually, separating darker and brighter spots. The former have stripe-like shapes with tiny pores and run perpendicular to the compaction direction; the latter have larger pores with very misaligned walls and shiny features. This distinction becomes more apparent at higher magnification (Fig. 7a). The darker regions are composed of several compacted layers, attributed to bundles of microsheets (Fig. 7b), well-aligned with each other and separated by thin and elongated pores. They eventually become contact lines when the pores are fully compacted (Fig. 7c - d) and are evidence of the intrinsic discontinuity of the microstructure. The thickness of the microsheets did not show large dimensional variations: they ranged from 40 to 120 nm and correspond to 120 to 360 carbon basal planes, at least twice the values predicted by nitrogen adsorption and specific surface area estimation [41,48].

In the transition between the two regions (Fig. 7c), the microsheets deviate from the aligned state and branch with continuity until they become pore walls. The relative interlocking between adjacent worms is so effective that any discontinuity due to particle boundaries was not detected. The extreme flexibility of the sheets allows the particles to withstand large deformations without failure, so that during compaction they can fold into themselves and collapse producing very irregular pore contours. This confirms observations made in earlier work [26] about the presence of two types of regions, one with slightly oriented microsheets and one with highly wrinkled microsheets, each associated with a different deformation response to uniaxial compressive loading. In the following, the oriented and wrinkled regions will be referred to as *aligned* and *misaligned* regions, respectively.

The pores detected in the imaged domain are highlighted and superimposed on the original image in Fig. 8a. The good detection of the largest pore area in the misaligned regions was sometimes affected by ambiguous features, visible in the inner surfaces, and shine-through effects. Conversely, the smaller pores area in the aligned regions was detected more accurately, although special care was required to discard the noisy, dark shades often mistaken for pores. In total, 2681 pores were identified within an area of $27.62 \times 41.47 = 1145.5$ µm^2, resulting in a porosity of 0.15 ± 0.05. The big discrepancy with the porosity of

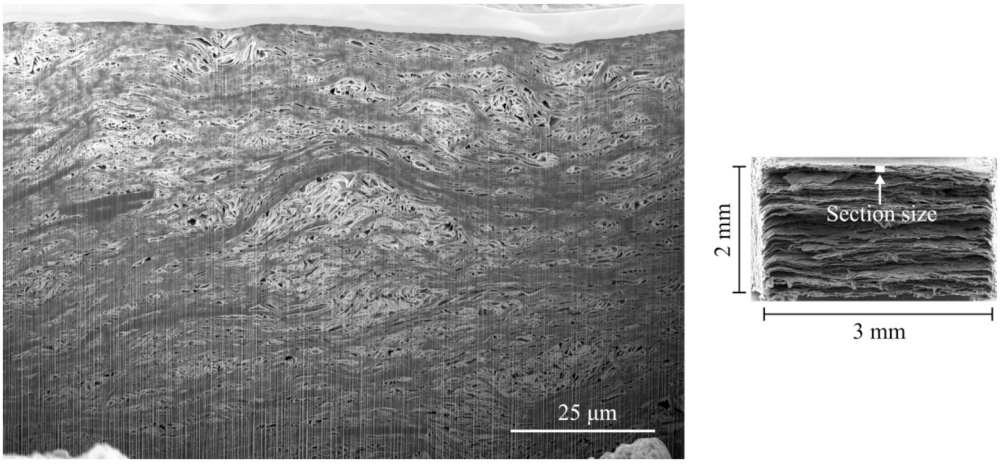

Fig. 6. Left: FIB-SEM section under investigation. Right: tension fractured specimen together with the actual dimension of the FIB-SEM section.

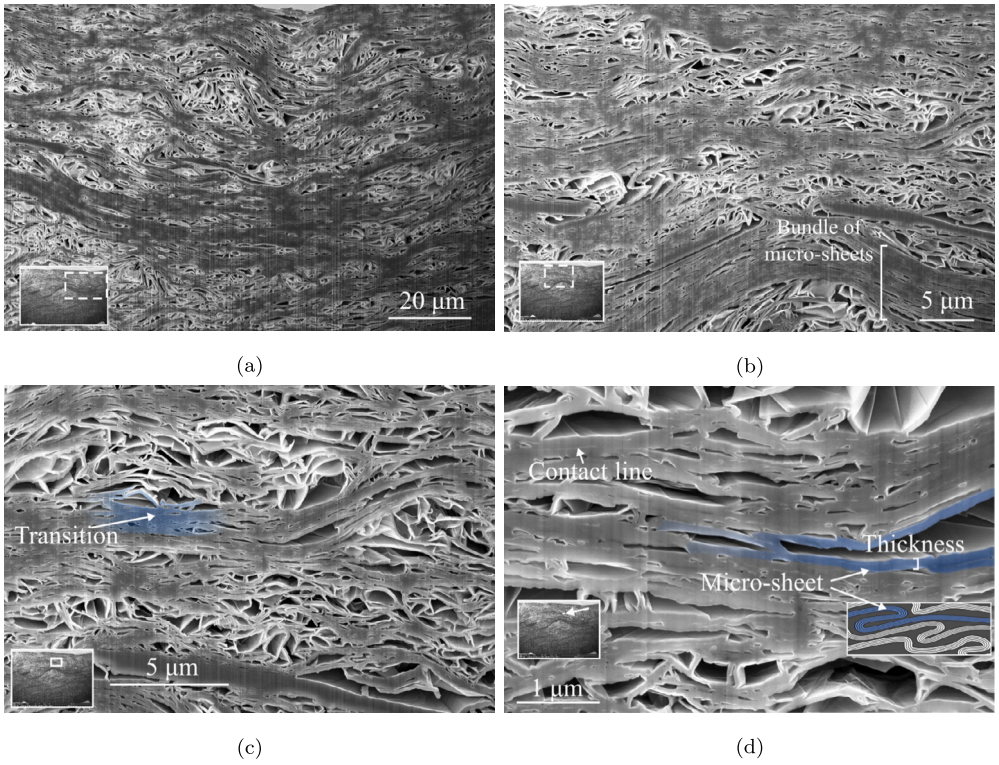

Fig. 7. Microstructure of Sigraflex® : magnified views.

the bulk material ($P = 0.51 - 0.55$) can be explained either by the local, two-dimensional nature of the investigation or by the density gradient along the thickness of the specimen, predicted in previous work [61], which implies a denser layer on the sheet surface.

The fraction of the aligned phase area to the total area (Fig. 8b) was between 0.42 and 0.55, with an average value of 0.49 corresponding to a porosity of 0.051, an order of magnitude lower than the porosity of the misaligned phase, which was about 0.24. The number of pores was similarly distributed between the two phases i.e., 1459 for the misaligned phase and 1222 for the aligned phase, although the former contributed 85% of the total porosity. The frequency counts corresponding to the pore properties studied are shown in Fig. 9 for both all pores and maintaining the separation between the aligned and misaligned regions. The corresponding numerical values are instead reported in Table 2. The characteristic pore size for all pores is 0.129 µm, in agreement with the characteristic pore size of macro-pores reported in a previous work [40], i.e. 0.08 µm. For the only misaligned regions this resulted 0.1451, two times larger than 0.0693 for the aligned regions.

The distribution in Fig. 9a shows pores that range from 0.0482 to 1.014 µm, corresponding to areas from 0.0073 µm^2 to 3.23 µm^2. Although the expected values of R_{ins} and R_{max} for the two phases are remarkably different, the expected value of AR and its distribution are almost identical for both phases. AR ranges around 0.38 for all pores, consistent with the expectation of flat, disk-shaped pores in a wide range of FG density [53]. This also implies that the difference between the two phases concerns only the pore size and that, assuming that misaligned regions turn into aligned regions at later stages of compaction, the mechanism of pore closure remains the same in all stages of compaction.

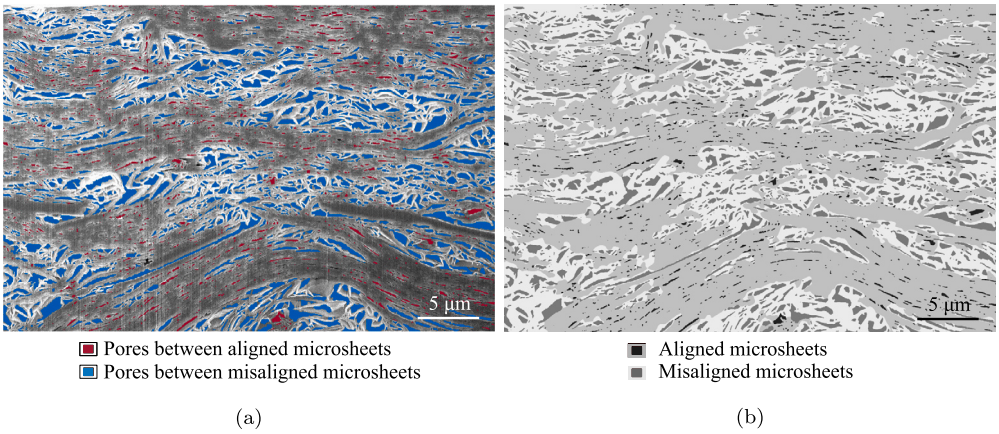

Fig. 8. Pores detected by image analysis: (a) pores highlighted and superposed to the original image, (b) aligned and misaligned phases with their respective pores.

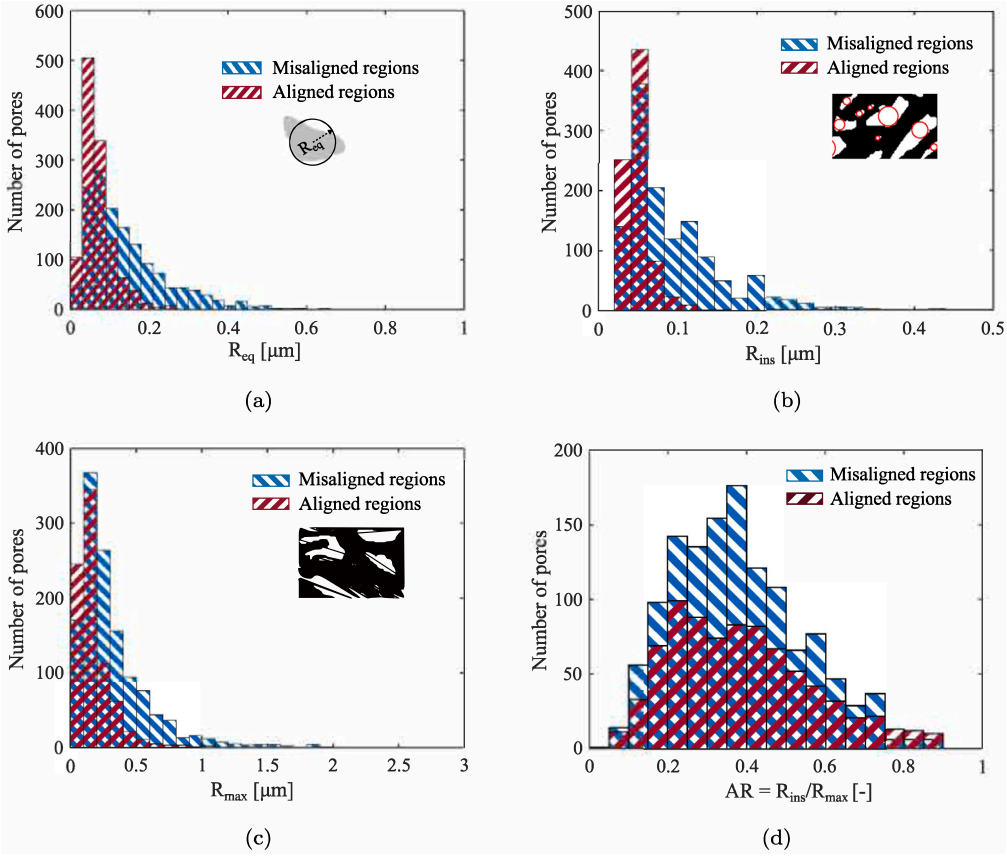

Fig. 9. (a) Maximum inscribed circle radii R_{ins} distribution, (b) half of maximum Feret diameter R_{max} distribution, (c) aspect ratio AR distribution, defined as fraction of the previous two quantities and (d) pore equivalent radii distribution.

Table 2
Mean values of pore parameters fitted by a log-normal probability distribution function. See Appendix B for definition of parameters.

Regions	All			Aligned			Misaligned		
Parameters	μ	$\bar{\sigma}$	Expected value	μ	$\bar{\sigma}$	Expected value	μ	$\bar{\sigma}$	Expected value
R_{eq} [μm]	-2.216	0.5776	0.129	-2.8219	0.5528	0.0693	-2.198	0.7319	0.1451
R_{ins} [μm]	-2.68	0.522	0.0786	-2.9727	0.3272	0.054	-2.495	0.5374	0.0953
R_{max} [μm]	-1.616	0.7234	0.2581	-1.923	0.577	0.1727	-1.422	0.74	0.3171
AR [-]	-1.064	0.4815	0.3875	-1.05	0.496	0.396	-1.073	0.4721	0.3824

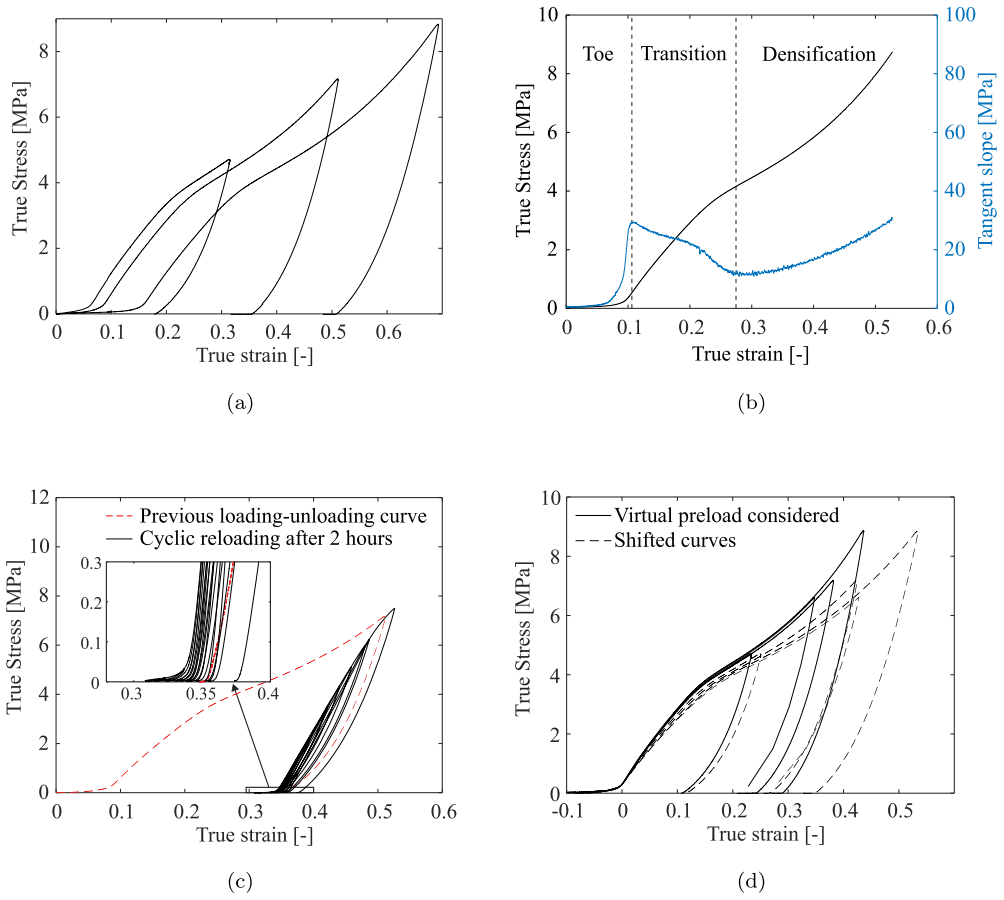

Fig. 10. (a) Uniaxial compression curves of Sigraflex® , together with top and side views of specimens obtained before compression and after recovery, (b) average curve and corresponding tangent slope, (c) monotonic loading up to 7 MPa and subsequent cyclic reloading after full recovery, (d) comparison of the curves obtained by shifting the strain axis and those obtained by assuming zero true stress at the virtual preload of 0.3 MPa.

4.2. Out-of-plane compression

Monotonic curves

Three examples of monotonic σ-ε curves are shown in Fig. 10a. Three domains were defined based on the behavior of the tangent slope in Fig. 10b. The first domain shows an initial non-linear toe, characterized by a fast increase in the absolute value of the tangent slope up to 30 MPa; while the true strain at this point showed a wide scatter of values around 6 – 6.2%, ranging between 1.5% and 16%, the corresponding stress values were tight within the range 0.3 - 0.4 MPa. Although this response is coherent to the low-load curves reported in a previous work (see Fig. 4 in the reference [28]), it was not excluded to be an effect of unexpected geometric imperfections of the specimens. To exclude it, a single sheet was monotonically loaded up to 7 MPa to obtain a perfectly flat specimen, allowed to recover for 2 hours, and finally loaded again, cyclically, up to 7 MPa (Fig. 10c). The toe was still visible, but the strain recovered was much lower than the one observed in the first loading-unloading path. The same behavior was also well visible in the piled-up specimens and was considered as part of the material response in a recent investigation of similar FG stacked disks loaded up to 1 MPa [28]. However, since it contributes to a large part of the total true strain, its was quantified by applying a virtual preload of 0.3 MPa to all the tests, and taking the corresponding displacement as a new zero for the definition (1). The curves obtained in this way tend to overlap nicely (Fig. 10d), conversely to the curves obtained by a simple backward shift along the strain axis, meaning that the specimen thickness starts to be *effective* only at the end of the toe. The reasons behind this phenomenon will be addressed in section 5 while here it is simply reported that the data analysis shown in the next section was based on the only curves with virtual preload applied.

The second domain is considered as a transition domain between the toe and the densification regime. Here the tangent slope decreases more slowly than in the first domain and reaches its local minimum at around 12 MPa in correspondence of $\varepsilon \approx 24\%$. The minimun occurs shortly after the knee of the σ-ε curves that corresponds to the hump visible in the transition range of the tangent slope curve. The stress corresponding to the slope minimum was $\sigma \approx 5.1$ MPa, again quite similar for all the tests.

In the third region, the tangent slope increased up to the maximum load while the concavity of the σ-ε curve turns upward. This trend was attributed to the densification regime due to the pore closures where the pore walls are predominantly touching with each other and there is probably a predominance of aligned regions.

Lastly, no sign of failure was observed within the range of stress tested, i.e. $\sigma \leq 14$ MPa.

Cyclic curves

An example of cyclic curve is shown in Fig. 11a. Those tests that were cyclically preloaded did not show any remarkable difference with the other ones and their curves were also used for the calculation of the cyclic tangent modulus. The cyclic paths stabilized after 2 - 6 cycles (Fig. 11b) while the toe was always visible in the low-load domain along with a constant area within cycles. In general, three main phenomena were visible in the cyclic curves: (i) memory of subsequent cycles σ-ε extreme points, (ii) nearly-zero yield strength and (iii) large hysteresis in the unloading-reloading path.

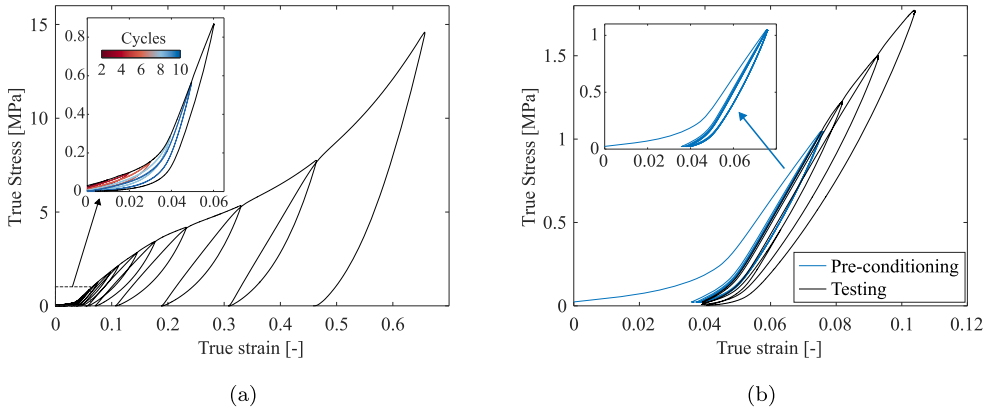

Fig. 11. Cyclic curves: (a) example of cyclic curve, including a magnification view of the first cycles at low loads. Two cycles at the same peak strain were done only up to $\varepsilon = 5\%$; (b) Stabilization at 1 MPa peak stress and cyclic loading at higher peak strains. The material has almost perfect memory of σ-ε extremals from the second cycle on.

The first one refers to the tests where two or more cycles were done at the same peak strain (Fig. 11a or inset in Fig. 11b). Inelastic deformation is induced in the material only during the first few loading cycles that are followed by a stable regime where the strain is fully recovered at each cycle. Hysteresis is always visible, but the σ-ε reversal points are held fixed and become memory points. The memory can be established again by exceeding the current peak stress and loading at higher strains. The second aspect involves the incapacity of finding a clear value of transition between the elastic and inelastic regimes. As shown in the inset of Fig. 11a, the cyclic path usually starts from a positive preload, around 0.03 – 0.04 MPa, reaches the cycle peak stress and finally recovers the total strain imposed. This is repeated until the peak stress does not overcome 0.5 MPa, where the inelastic strain at zero load appears. However, for any peak stress, also lower than 0.5 MPa, the stress values at zero strain tend to decrease as if the preload value was already exceeding the yield strength. Although this phenomenon was already observed in different types of graphite, it may also be due to the viscoelastic nature, and thus waiting a longer recovery time at zero load may allow for full elastic recovery (see section 5 for further discussion). It is noted that not marked differences were observed in the behavior of the slowest test at 0.01 mm/min. The hysteresis is evidenced by the large difference between the loading and unloading path; during each loading the curve shows the initial toe, followed by a nearly linear path that is somewhat analogous to the transition region of the monotonic curves. The unloading path is instead highly nonlinear, and the toe tends to gradually become shorter at increasing loads, until almost disappearing completely when $\sigma > 7$ MPa.

Initial cyclic tangent modulus

The uniaxial compression test can be considered as a sort of continuation of the production process, and each unloading as the final stage for obtaining a new sheet with higher density. Part of the new irreversible deformation is due to further folding and interlocking of microsheets which affect the shape and size of the pores and, consequently, the elastic response for which the initial tangent modulus H is representative. While in metals, polymers and cement foams, the secant elastic gradient usually vary according to the elastic, plastic and densification domains [60], the initial tangent modulus of Sigraflex® increases only monotonically in the whole stress domain (Fig. 12a). The material hence undergoes stiffening from the beginning of compaction, with an initial value of the modulus around 30.35 MPa at $\rho_p^* = 0.43$ that increases up to 62.3 MPa at $\rho_p^* = 0.6$, continuing the crumpling process from where it was left after production.

To describe the evolution of the elastic modulus of expanded graphite compacts over a wide range of densities up to 1 g/cm^3, an exponential law was proposed in a previous work [53]. Not only, but also the relation between the compaction stress σ_p and the final density ρ_p of FG sheets can be described by an exponential law of the type [28]:

$$\sigma_p = 0.35\, e^{2.6\rho_p} \quad \text{or, by setting } \rho_p = \rho_p^*\, \rho_s, \quad \sigma_p = 0.35\, e^{5.88\rho_p^*} \tag{3}$$

In light of these observations, the cyclic tangent moduli were plotted in semilogarithmic coordinates (Fig. 12b) along with different data available in literature, and both fitted by non-linear least square regression with exponential functions of the type

$$H = H_0\, e^{n\rho_p^*}, \tag{4}$$

where H_0 is H at $\rho = \rho_0$, and n is the exponential coefficient. The fitting captures the evolution of the moduli rather well, and the similarity between the exponential coefficients obtained for the initial cyclic tangent modulus (3.4) and the elastic moduli derived from literature data (3.89) supports the idea that the application of additional out-of-plane compression can be interpreted as a continuation of the production process. Even if the data compared were obtained on specimens tested under different conditions (closed die or rolling) and measured with techniques (ultrasound speed or stress-strain tangent slope), it is clear that the stress and tangent modulus of FG follows exponential scaling laws of the type (3) and (4), at least when the relative density is in the range 0.1 – 0.2 g/cm^3 $\leq \rho_p^* \leq$ 0.7 - 0.8 g/cm^3.

Residual deformation

In Fig. 13a, the measurements of the thickness and radius at the end of each test divided by the initial values are shown against the maximum true strain. The resolution of the calliper was enough to exclude the influence of a systematic error, but not to resolute the size variations of specimens loaded below a true strain of 0.08. The axial residual strain along the thickness was also compared with the corresponding machine log data recorded at the end of the unloading paths. This was done to assess any difference between the thickness at the end of the test and after long-time relaxation (detected by the calliper). The latter was more effective at strain higher than 0.5 where larger gaps are visible between the calliper and machine data. The radial residual strains rose above the calliper resolution around a true strain of 0.1 (corresponding to 3 MPa) and increased almost linearly with the applied deformation.

It was also observed (inset of Fig. 13a) that the surfaces between the individual disks of piled-up specimens developed a rippled texture as a result of the highly effective friction forces acting between them. The ratio between the residual strains in the radial and axial directions reported in Fig. 13b can be considered as a first estimation of the plastic Poisson's ratio of the material. The value found here (0.083) is constant up to $\varepsilon \approx 0.6$, and compares quite well with typical values of foams and cellular materials, (≈ 0.04 [64]), and with the elastic Poisson's ratio of a single FG particle (0.04) subjected to compressive deformation [49].

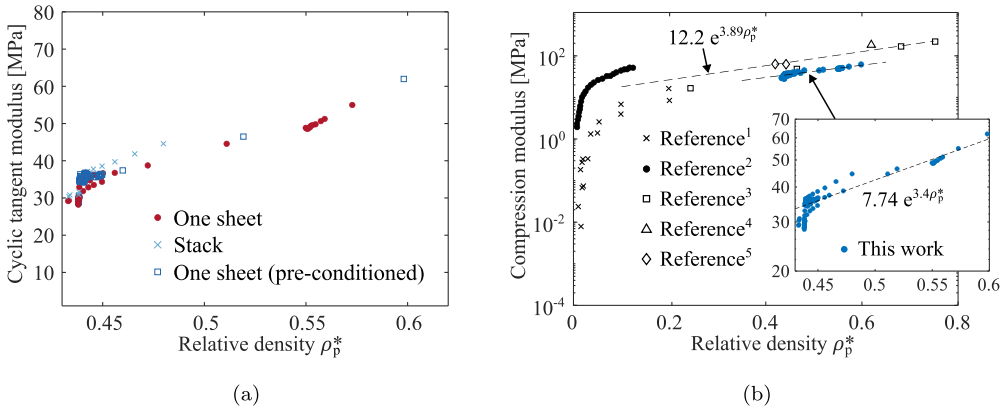

Fig. 12. (a) Initial cyclic tangent modulus of the loading cycles, (b) literature data for elastic compression moduli vs relative density including data from literature: [1] [62], [2] [41], [3] [28], [4] [63], [5] [53]. The moduli were measured by ultrasound speed or stress-strain tangent slope. Here, only data points corresponding to $\rho_p^* > 0.1$ were considered in the regression.

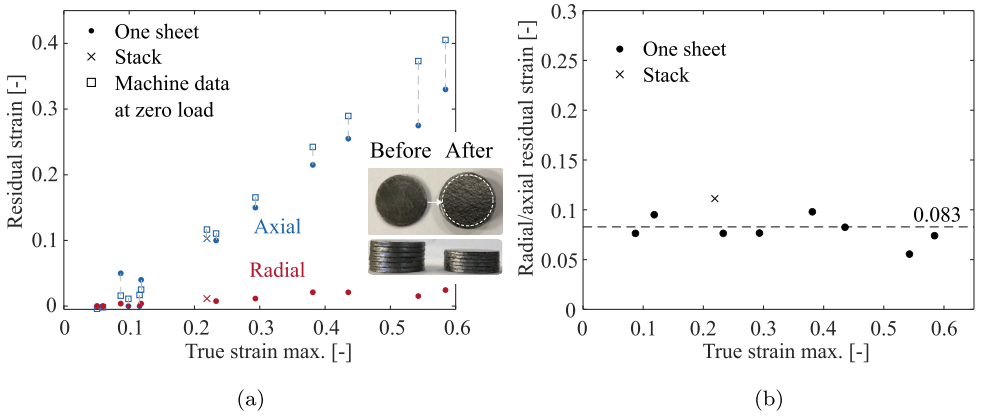

Fig. 13. (a) Radial and axial residual strains, and (b) radial/axial residual strain ratio. The measures of the sample thickness were taken by a digital calliper at least 30 minutes after each test and compared with the machine displacement in (b). The latter represents the values of the thickness as soon as the test was ended, while the dashes lines represent the waiting time before each measurement (≥ 30 minutes).

The low volumetric change shown, regardless of the large strain, justifies the assumption made in Eq. (2) and allows the volumetric strain to be approximated by the axial strain for both single and stacked specimens.

5. Discussion

5.1. FG as a crumpled material

Thanks to FIB-SEM imaging, it is clear that FG has a complex pore space originated by irreversible crumpling of microsheets essentially constituted of hundreds of carbon basal planes. Considering that the elastic modulus perpendicular to the basal plane of a graphite single crystal (usually denoted by c-axis) is $C_{33} = 36.5$ GPa [65], and that the out-of-plane elastic modulus of a less perfect material such as polycrystalline or pyrolytic graphite ranges from 10.88 GPa to 29.35 GPa [66,67], a simple rule of mixture would estimate the out-of-plane modulus $E_\perp$ of FG in the range $1 - 10$ GPa, that is at least a hundred times larger than the actual FG tangent modulus. A good explanation to this discrepancy can be given by regarding FG as having a crumpled mesostructure, in which the bending mechanism of the microsheets plays the major role under compression loads. Indeed, if the agglomerated compact of exfoliated graphite at low relative densities is approximated as a honeycomb cell structure and the deformations are taken as elastic, the ratio between the elastic modulus of the bulk compact E^* and the solid part E_s scales with a power law of the type $E^*/E_s \approx (h/L)^3$, where h and L are the thickness and length of a cell wall [64]. For a microsheet with $h \approx 0.4 - 0.12$ μm and $L \approx 10 - 32$ μm, such ratio is estimated in the order of $10^{-8} - 10^{-6}$. Assuming further that E_s corresponds to the graphite single crystal in-plane modulus $C_{11} = 1060$ GPa because of dominant bending, [65] then $E^* \approx 10^{-2} - 1$ MPa provides a much better estimate for the elastic modulus of compressed expanded graphite at low relative density reported in Fig. 12b. At relative density higher than $0.1 - 0.2$ however, the ratio E^*/E_s changes behavior and scales exponentially with the relative density, and hence with the ratio h/L (for honeycomb cells, the last two quantities are proportional [64]. This change may be explained by the folding mechanisms observed in crumpled materials that differs substantially from deformation mechanisms of cellular materials. Therefore, FG can be modeled as a crumpled material in which many microsheets (and not just a single thin sheet) are crumpled at the same time. These undergo severe distortion made possible by the very low shear forces needed to delaminate the microsheets, and by the ability of the carbon planes to form sharp curves without breaking [68]. The analogy with crumpled materials may also explain:

- the random formation of aligned and misaligned regions. The nonuniform distribution of mass and voids is random as when a paper ball is crumpled under compressive forces [69],
- the huge volumetric strain undergone by the pores during the compaction. These, in the uncompacted worms, have wall-to-wall size of the order of ≈ 10 μm, whereas the average size of a Sigraflex® pore ranges around 0.1 μm. This leads to a large volumetric strain that implies a substantial change in pore space with continuous

folding of the microsheets and creation of new pores among the folds,
- the impossibility of compacting a FG sheet to $\rho > 1.9$ g/cm^3. The crumpling process is indeed governed by a material property called fractal dimension D ($2 < D < 3$ [70]) that quantifies the packing efficiency of a specific thin material ($D = 3$ for effective packing). For single layer graphene, it was found $D = 2.36$ [71] that implies a weak efficiency in the crumpling process potentially reflected in the behavior of microsheets,
- the excellent reproducibility of the stress-strain curves (once the contribution of the toe is eliminated). Although the apparent random formation indeed, the statistical properties of crumpled materials exhibit excellent reproducibility [72].

5.2. Compression curve of FG and crumpled materials

The initial nonlinear toe observed in Fig. 10b is a feature reported in previous investigations about crumpled and entangled materials [31,73–75,29]. This regime was described as *apparent*, resulting from two deformation contributions, one from the material and the other from dry sliding between sheets, i.e. the mesostructure. In analogy, this allows to think of FG initial toe as a combination of material and structural contributions: the first is localized near the creases and involves basal dislocations inside the microsheets, while the second can be associated to local rigid motions of undeformed microsheets that result on large macroscopical deformation. It is therefore suggested that the toe strain is due to the relaxation of the material after the production process governed by meso-structural mechanisms such as microsheets sliding and unfolding.

The transition domain (Fig. 10b) can be interpreted as a hardening region, as opposed to the typical flat plateau visible in foams compression due to the buckling of cell walls. Hardening and the absence of a flat plateau were also observed in crumpled aluminum [30] and were motivated by noticing that the stress increases with the number of contact points according to a power-law-like dependence [31]. Here however, the FG transition domain shows downward concavity and it is suggested that this may originate from the aligned regions, where the probability of new contacts is reduced, and the deformation mechanism is closer to that of crystalline graphite.

The stress-relative density relation in the densification regime follows an exponential law of the type (4). This may originate from the ability of the microsheets to fold more severely than other materials and hence to form more and more hard-to-bend ridges that motivate the stiffness and strength increase [68].

Finally, differences between FG and crumpled materials under compression can be related to the nature of the base material, that is, for example in crumpled aluminum the yield point is obvious and the hysteresis area is very limited, where FG has unclear yield stress and large hysteresis loops areas. Indeed, the nearly-zero yield strength is well-known to occur naturally in polycrystalline graphite under uniaxial compression loads [76] while the viscous character of FG [48] may be inherited by the layered crystal structure of graphite. This allows basal dislocations and incipient kink bands to propagate and exhibit recoverable hysteresis loops [77] as well as memory of the extremal points of the loops more typical of soil and rocks [78].

6. 1D analytical model

Intuitively, the aligned regions tend to arrange themselves in an orderly manner at increasing compression forces; their local response is expected to be increasingly stiff, predominantly due to the dislocation mechanisms of the crystalline structure and responsible for the reversible energy stored in the material (also suggested in a previous work [26]). In contrast, misaligned regions contribute mainly to the inelastic deformation through their mesostructure, which creates new folds and interlocking constraints. Once sufficiently crumpled, these regions can be considered as aligned, and begin to contribute to the elastic response, resulting in an overall stiffening and shifting of the dominant deformation mechanism from the mesostructure to the microstructure. In this section, a simple analytical model is proposed in an attempt to decouple the deformation mechanisms of the graphitic component, associated with the aligned regions, and the crumpled component, associated with the misaligned regions.

The aligned regions are here associated to a stress-strain response similar to polycrystalline graphite under compression. This was found to obey a power law of the type [79]:

$$\varepsilon = A\sigma + B\sigma^2, \tag{5}$$

where A [MPa^{-1}] and B [MPa^{-2}] are defined as elastic and plastic compliances. The model originated from the intuition of inhomogeneous plastic deformations that gradually participate to the overall deformation and can be visualized as a continuous involvement of additional spring in series. Despite the equation was found to give a good fit only up to a half of the graphite sample strength, this is easy to manipulate and resembles the commonly used Ramberg-Osgood equation when the stress exponent is set to 2. This can be expressed in terms of stiffnesses instead of compliances as:

$$\varepsilon = \varepsilon_e + \varepsilon_p = \frac{\sigma}{E_0} + \frac{\sigma^2}{K}. \tag{6}$$

Here E_0 is the elastic modulus of the aligned regions at zero strain and K is a material parameter that accounts for both the volume fraction and stiffness of the aligned regions involved in the plastic deformation. This relation can also be inverted, assuming positive strain $\varepsilon \geq 0$, as follows:

$$\sigma = -\frac{K}{2E_0} + \frac{K}{2E_0}\left(1 + \frac{4E_0^2}{K}\varepsilon\right)^{1/2} \tag{7}$$

On the other side, the misaligned regions are associated to a different function of the compressive stress and the *current* relative density ρ^*. This differs from ρ_p^* defined in Eq. (2) since it is related directly to ε by:

$$\rho^* = \frac{\rho_0}{\rho_s} e^{\varepsilon}. \tag{8}$$

To formulate the final relationship, it is now assumed that Eq. (4) is valid not only for ρ_p^*, but also for ρ^*. This is supported by the fact that, by analogy, plotting the experimental σ - ρ^* curves (Fig. 14a) in semi-logarithmic coordinates, a straight line could be fit in the whole densification regime. The σ - ρ_p^* curves were also plotted for comparison in the same figure. As expected, the exponential coefficient is in a good agreement with that reported in Eq. (3), i.e., 5.88, and the difference is ascribed to the uncertainty about the real relative density of tested specimens in this work. Therefore, the contribution of the misaligned regions to the overall compressive modulus can be related to ρ^* by Eq. (4) just by replacing ρ_p^* with ρ^*:

$$H = H_0 e^{n\rho^*}. \tag{9}$$

Relation (9) cam be easily expressed in terms of ε by use of (8):

$$H = H_0 e^{n\frac{\rho_0}{\rho_s}e^{\varepsilon}}. \tag{10}$$

The contributions from (7) and (10) are assumed to work in parallel as shown in the equivalent rheological model of Fig. 14b, and the total stress σ versus true strain ε relationship reads:

$$\sigma = -\frac{K}{2E_0} + \frac{K}{2E_0}\left(1 + \frac{4E_0^2}{K}\varepsilon\right)^{1/2} + H_0 e^{n\frac{\rho_0}{\rho_s}e^{\varepsilon}}\varepsilon, \tag{11}$$

Eq. (11) was used to fit the average experimental monotonic curves in the range $0 \leq \varepsilon \leq 0.6$, corresponding to $0 \leq \rho_p^* \leq 0.6$, as shown in Fig. 14b. The statistics of the fitting parameters is reported in Table 3 together

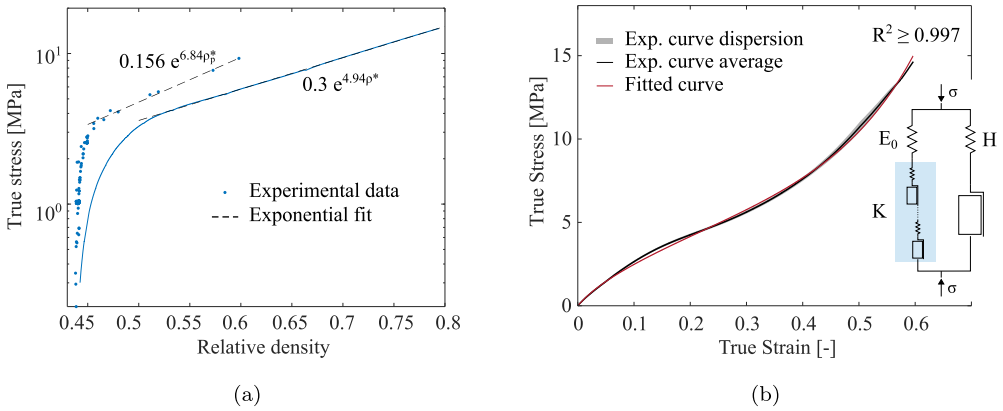

Fig. 14. (a) True stress vs relative density curves. Both ρ^* and ρ_p^* are used as independent variable. (b) Example of experimental curve fitting by means of Eq. (11), including a schematic view of the proposed rheological model.

Table 3
Statistics of fitting parameters obtained by the mechanical model of Eq. (11).

	Median	95% confidence interval
E_0 [MPa]	39.41	(fixed)
H_0 [MPa]	0.04262	(0.0392, 0.04604)
K [MPa^2]	135	(133.2, 136.7)
n [-]	7.091	(6.995, 7.187)

with the corresponding confidence interval. The parameter E_0 was obtained a priori from a high order polynomial fitting of the average curve, whose slope was evaluated at $\varepsilon = 0$, and it was kept fixed during the fitting. Whereas the exponential trend in the densification regime is matched perfectly, much room for improvement is visible in the transition region: this indeed depends on the exponent 1/2 in Eq. (7) which is already known to partially match the graphite behavior. The friction blocks in the rheological model of Fig. 14b were inserted only to represent the accumulated inelastic strain and to underline that both the graphitic and crumpled natures give separate contributions to the overall inelastic deformation. The ones backing the series of springs associated to the fitting parameter K represent the non-recovered deformation derived from dislocations internal to the micro-sheets. Although in the original model for polycrystalline graphite, each spring of the spring series was associated to the elastic stiffness of the plasticizing regions [79], here these components were not decoupled, and all the equivalent contribution is gathered in the single fitting parameter K. On the other side, the friction block backing the spring H represents the contact forces at microsheets interlocks and hence all the meso-structural contributions.

Despite a 1D model is not comprehensive and direct applications for material modeling are limited to the reproduction of the 1D stress-strain response (for example for the input in the material models of finite element software), it confirms that the assumptions made about the decoupling of deformation contributions are realistic.

7. Conclusion

The problem of FG constitutive modeling is relevant for the prediction of performances of current and future applications, including the TDE. This is a complex task that needs to be broken down and addressed in stages, for which this research represents a fundamental one. Here, the microstructure of Sigraflex® ($\rho = 1$ g/cm^3) is investigated, with a particular focus on quantitative properties of pore space, as well as its uniaxial compression properties in the out-of-plane direction. The key findings for Sigraflex® are listed below and can be considered valid for FG with similar density and production parameters:

1. FIB-SEM technique has proven effective for microstructure characterization of FG and is considered extremely valuable for future 3D microstructure reconstruction by, for example, FIB-SEM tomography.
2. The microsheets were clearly visible and estimated to be made of 120 - 360 carbon basal planes. Regions of aligned and misaligned microsheets constitute the FG microstructure: the first ones are composed of bundles of well-oriented microsheets surrounded by thin and elongated pores. The second ones have bigger pores and mainly contributed to 85% of the overall porosity. All the pores were found to have low aspect ratio (0.384), consistently with previous works [53] that suggested flat, disk-shaped pores, and had characteristic pore size of 0.129 μm.
3. Three stages of deformation were found in the monotonic stress-strain curves: the initial toe, the transition and densification regime. The deformation mechanism behind the initial toe was attributed to a structural component of the strain due to the relaxation of microsheets after the compaction. The transition region was similar to a hardening regime with downward concavity attributed to the predominance of graphite-like dislocation mechanism. The exponential behavior developed under densification was attributed to the formation of folds that become increasingly hard to bend under compaction.
4. During the cyclic loading, FG showed memory of the extreme points of the cycles, similar to rock and soils, nearly zero yield strength typical of graphitic material, and large loop hysteresis. The initial cyclic tangent slope was related to the residual relative density by an exponential law.
5. An approximation of the plastic Poisson's ratio was found to be 0.083.
6. Many aspects of FG mechanical response were in common with crushable foams and especially crumpled materials. The crumpled nature can explain the initial toe visible in the monotonic curves, the random formation of aligned and misaligned regions, the large volumetric strain undergone by the pores during the compaction, the impossibility of compacting a FG sheet to $\rho > 1.9$ g/cm^3, and the excellent reproducibility of the experimental curves.
7. the 1D phenomenological model was proposed, and the matching with the average stress-strain curve was quite satisfactory. This supports the assumptions that the aligned regions behave like crystalline graphite and the crumpling of misaligned regions contribute to the overall stiffening during compaction. The analytical curve can be used to model FG out-of-plane response, e.g. in finite element software, and perhaps extrapolate the trend at relative density higher than 0.6.

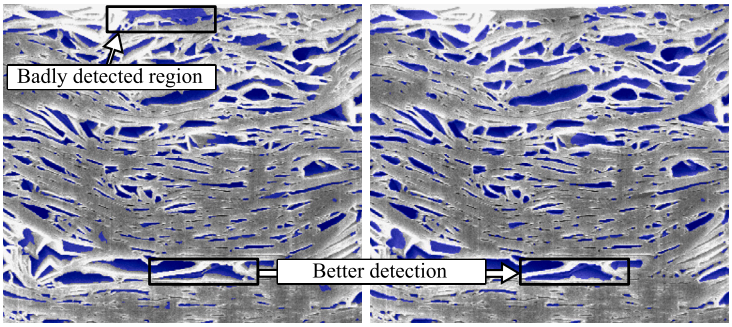

Fig. 15. Left: image binarized before watershed segmentation. Right: image binarized after edge detection and watershed segmentation.

Declaration of competing interest

The authors declare that they have no known competing financial interests or personal relationships that could have appeared to influence the work reported in this paper.

Data availability

Data will be made available on request.

Acknowledgements

This work made use of NTNU laboratories: Realization Laboratory, Nanomechanical Testing Laboratory, Fatigue, Fracture and Mechanical Characterization Laboratory, and NanoLab. The authors are also thankful to Malin Alette Lervaag and Tore Andre Kristensen for technical support. E. Solfiti thanks prof. O. S. Hopperstad for constructive discussions and suggestions.

Appendix A

Segmentation procedure

The SEM image segmentation was performed in MATLAB® using Image processing Toolbox™. For detailed information, the reader is referred to the online support of such toolbox.[1] It was observed that the thin and tiny pores were easy to capture by simple global thresholding and binarization, while large pores were badly detected due to visible internal features. To improve the detection of large pores, a marker-controlled watershed transform was employed. The procedure is as follows:

1. import grayscale image and apply anisotropic diffusion filter. This preserves the pore edges while reducing the noise,
2. apply morphological operations such as erosion, dilation, opening and closing, to regularize the pore contours,
3. detect pore edges,
4. apply binarization to the image obtained in step 2 using a global threshold computed with Otsu's method. Doing like this, at least one marker per each pore is obtained,
5. combine markers and edges in one image and apply watershed segmentation.

Tiling of the images was also done in order to optimize locally the accuracy of binarization. An example of image tile is shown in Fig. 15 before and after the procedure above. Morphological operations improved the analysis and manual intervention was sporadically needed to discard poorly detected pores, sometimes confused with dark artifacts in the denser material domains. Pores smaller than 10 pixels were also discarded. All the quantities calculated were converted to the metric system by pixel proportion.

The second stage of image analysis involves separating the aligned phase from the misaligned phase and attributing the pores to one or the other. This relies on the 2D Fourier transform and hence on the assumption that the two phases show different frequencies of darker and brighter spots. The stage consists on the following steps:

1. compute 2D Fourier transform of grayscale image. The amplitude (logarithmic scale) is shown in Fig. 16a,
2. apply passband filter to the transform, as in Fig. 16b,
3. reconstruct the image and binarize using a global threshold computed with Otsu's method (Fig. 16c and d).

Several optimal frequency bands are chosen by visually overlaying the original and binarized images. For each band, the set of pores obtained in the initial phase is checked whether it belongs to one or the other phase. If more than 50% of the pore area (in pixels) overlaps with a phase, then the pore belongs to that phase. The parameters reported in Table 2 and the total porosity are finally obtained as the average of the characteristic pore parameters over all the frequency bands.

Appendix B

In Fig. 17, the fitted probability distribution functions of the parameters considered in Table 3 are reported. The definition of the log-normal probability distribution function used for each of the statistic parameters is as follows:

$$f(x;\mu,\bar{\sigma}) = \frac{1}{x\bar{\sigma}\sqrt{2\pi}} e^{-\frac{(\ln(x)-\mu)^2}{2\bar{\sigma}^2}},$$

where $x > 0$ is the random variable, μ is the mean of the logarithm of x, and $\bar{\sigma}$ is the standard deviation of the logarithm of x. The expected value $E[x]$ is obtained by $E[x] = e^{\mu+\frac{1}{2}\bar{\sigma}^2}$.

Appendix C

Observation of detached particles

This analysis was performed with the aim of investigate the similarities between FG and the class of materials of compacted powders. Indeed, FG is nothing else than an exfoliated graphite powder compact with soft particles that aggregate thanks to their mesostructure ability to fold and interlock. The role of cohesive forces is probably not observable under compression loads, while it may constitute the key contribution to model the mechanical response under tensile or simple shear loading. Density-dependent properties such as the elastic modulus are also common in compacted powders.

The particles detached from the specimen surface by scotch taping looked like the one in Fig. 18. It is not be possible to indicate with certainty whether the whole particle or part of it could be detached,

[1] https://se.mathworks.com/help/images/.

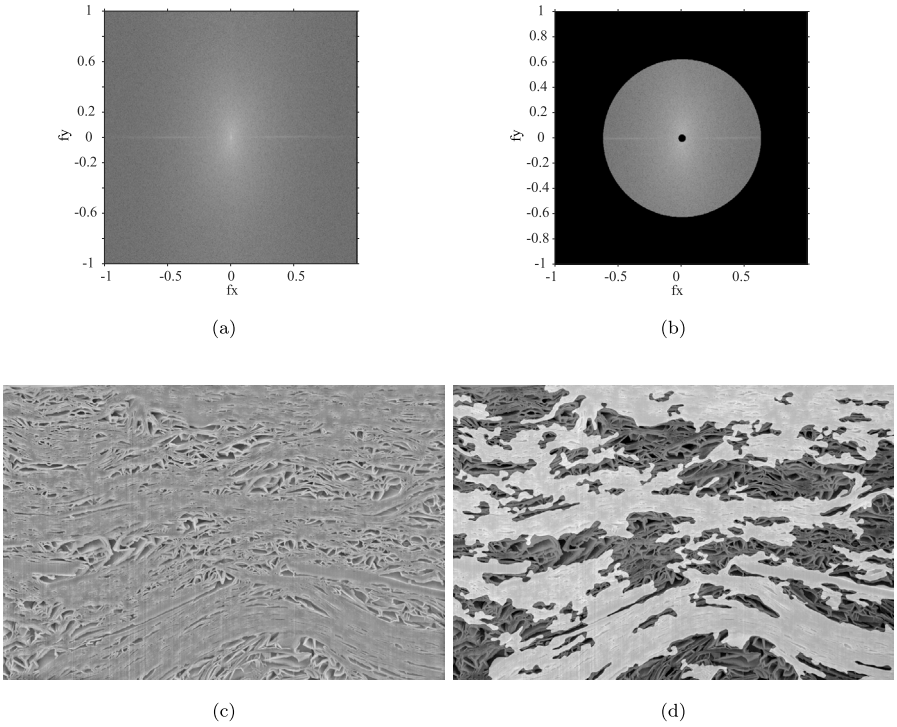

Fig. 16. Example of phase detection: (a) amplitude of 2D Fourier transform plotted along the 2D spatial frequencies *fx* and *fy*; (b) filtering of the transform; (c) images reconstructed after filtering; (d) overlaying of binary image corresponding to the aligned regions with the original image. The misaligned phase is taken as the complementary part of the aligned phase.

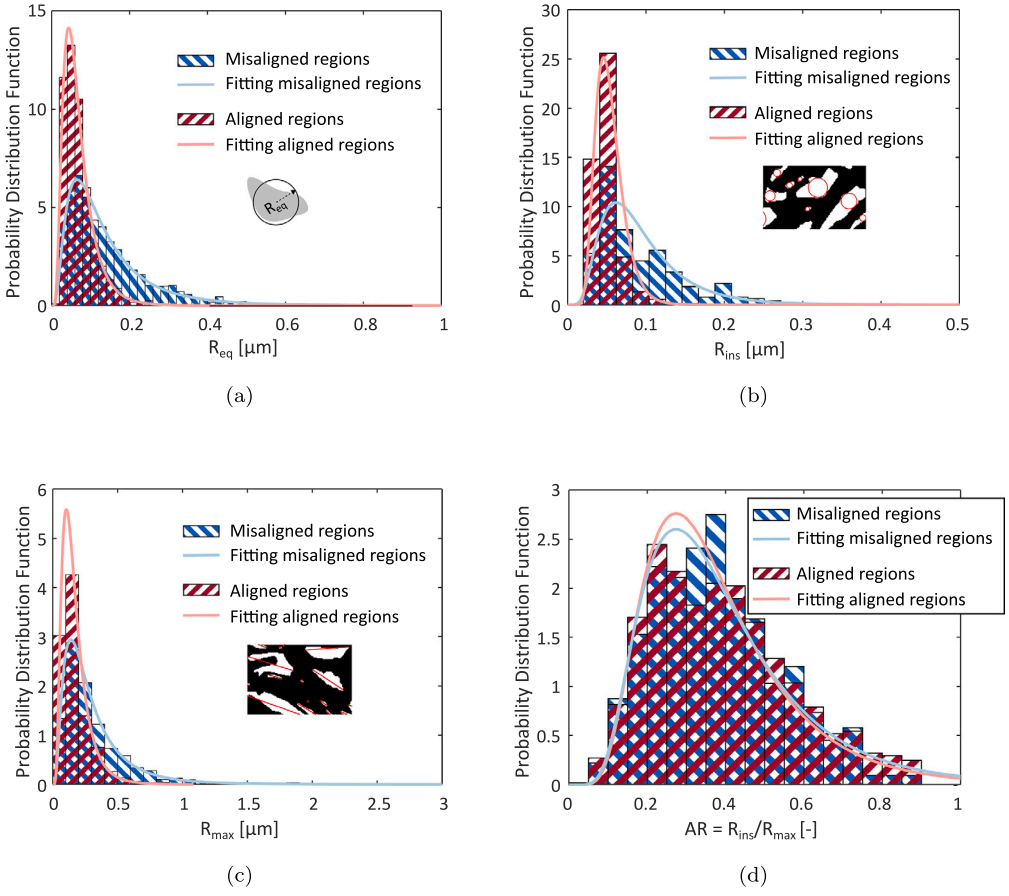

Fig. 17. Fitting of the lognormal probability distribution function to the parameters employed in the pores size and shape investigation.

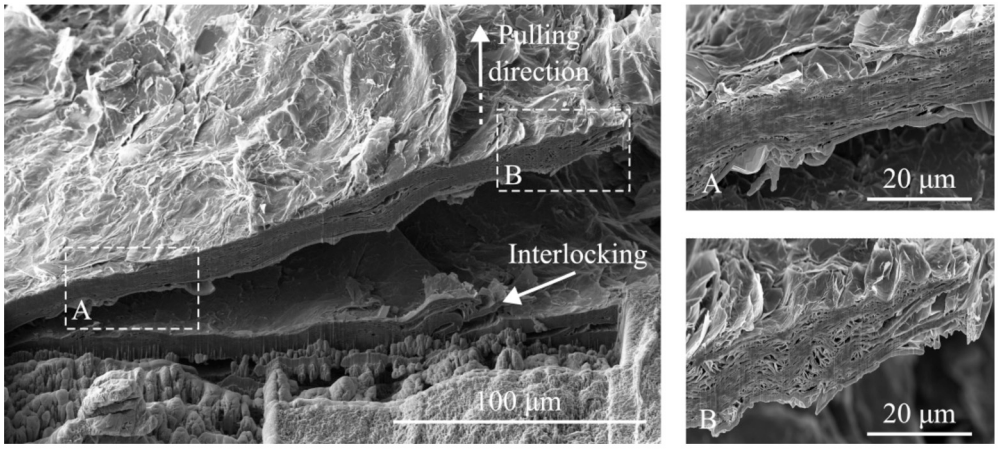

Fig. 18. FIB-SEM investigation of a particle detached from the specimen top surface. The magnification views show aligned and misaligned regions in the inner microstructure.

but the thickness size thereof is coherent with those expected for compressed particles. Many microsheets were torn apart and fractured in the out-of-plane direction, which corresponded with the pulling direction of the tape. A small part of the particle detached appear as still being attached to the bottom surface and constitutes as an example of how the particle interlocks among each other. However, once they are compacted together, it is nearly impossible to distinguish them since the inner and outer (in between the particles) porosity show the same level of inhomogeneity. Both aligned and misaligned regions are clearly visible in the inner particle structure and especially in the inset B of Fig. 18, the microsheets configuration appears as the result of mesostructure kinking due to in-plane compression stress. In this case, the misaligned regions are originated in between two kinking microsheets bundles.

References

[1] J. Heredia, A. Perillo-Marcone, F. Berto, A. Alvaro, K. Kershaw, D. Grenier, V. Rizzoglio, E. Solfiti, R. Franqueira Ximenes, F.-X. Nuiry, et al., Jacow: sigraflex® studies for lhc cern beam dump: summary and perspective, in: JACoW IPAC 2021, 2021, pp. 3571–3574.

[2] J.H. Shane, R.J. Russell, R.A. Bochman, Flexible graphite material of expanded particles compressed together, 1968, US Patent 3,404,061.

[3] D. Chung, A review of exfoliated graphite, J. Mater. Sci. 51 (2016) 554–568.

[4] P. Jaszak, Modeling of the elastic properties of compressed expanded graphite-a material used in spiral wound gaskets, Int. J. Press. Vessels Piping 187 (2020) 104158.

[5] SGL Carbon, Smart Solutions in Graphites & Fiber Composites, https://www.sglcarbon.com. (Accessed 8 November 2022).

[6] M. Cermak, Natural graphite sheet heat sinks for power electronics, Ph.D. thesis, Applied Sciences: School of Mechatronic Systems Engineering, 2020.

[7] J. Gandhi, A. Pathak, Performance Evaluation of Thermal Interface Material for Space Applications, Applied Mechanics and Materials, vol. 110, Trans Tech Publ, 2012, pp. 135–141.

[8] E. Marotta, S.J. Mazzuca, J. Norley, Thermal joint conductance for flexible graphite materials: analytical and experimental study, IEEE Trans. Compon. Packag. Technol. 28 (2005) 102–110.

[9] N. Sykam, G.M. Rao, Lightweight flexible graphite sheet for high-performance electromagnetic interference shielding, Mater. Lett. 233 (2018) 59–62.

[10] R. Chugh, D. Chung, Flexible graphite as a heating element, Carbon 40 (2002) 2285–2289.

[11] Y. Fu, M. Hou, X. Yan, Y. Fu, Z. Shao, Z. Hou, P. Ming, B. Yi, et al., The electrical resistance of flexible graphite as flowfield plate in proton exchange membrane fuel cells, Carbon 46 (2008) 19–23.

[12] M. Yazici, D. Krassowski, J. Prakash, Flexible graphite as battery anode and current collector, J. Power Sources 141 (2005) 171–176.

[13] X. Xi, D.D. Chung, Electret, piezoelectret, dielectricity and piezoresistivity discovered in exfoliated-graphite-based flexible graphite, with applications in mechanical sensing and electric powering, Carbon 150 (2019) 531–548.

[14] European Organization for Nuclear Research (CERN) - Large Hadron Collider (LHC), https://home.cern/science/accelerators/large-hadron-collider. (Accessed 22 May 2022).

[15] L. Evans, P. Bryant, L.H.C. machine, J. Instrum. 3 (2008) S08001.

[16] J. Wenninger, Machine protection and operation for LHC, arXiv preprint arXiv:1608.03113, 2016.

[17] F.-X. Nuiry, M. Calviani, M. Bergeret, S. Pianese, M. Butcher, L.-M. Grec, A. Lechner, M.I. Frankl, F.L. Maciariello, T. Pichon, 3d carbon/carbon composites for beam intercepting devices at cern, Mater. Des. Proces. Commun. 1 (2019) e33.

[18] J. Maestre, C. Torregrosa, K. Kershaw, C. Bracco, T. Coiffet, M. Ferrari, R.F. Ximenes, S. Gilardoni, D. Grenier, A. Lechner, et al., Design and behaviour of the Large Hadron Collider external beam dumps capable of receiving 539 MJ/dump, J. Instrum. 16 (2021) P11019.

[19] M. Khelifa, V. Fierro, J. Macutkevic, A. Celzard, Nanoindentation of flexible graphite: experimental versus simulation studies, Rev. Adv. Mater. Sci. 3 (2018).

[20] P. Jaszak, Adaptation of a highly compressible elastomeric material model to simulate compressed expanded graphite and its application in the optimization of a graphite-metallic structure, J. Braz. Soc. Mech. Sci. Eng. 42 (2020) 1–22.

[21] N. Nan, J. Wang, A.A. Eckstein, FIB-SEM three-dimensional tomography for characterization of carbon-based materials, Adv. Mater. Sci. Eng. (2019) 2019, https://doi.org/10.1155/2019/8680715.

[22] J.D. Arregui-Mena, P.D. Edmondson, A.A. Campbell, Y. Katoh, Site specific, high-resolution characterisation of porosity in graphite using fib-sem tomography, J. Nucl. Mater. 511 (2018) 164–173.

[23] A. Baux, G. Couégnat, G.L. Vignoles, D. Lasseux, A. Kuhn, C. Carucci, N. Mano, T.D. Le, Digitization and image-based structure-properties relationship evaluation of a porous gold micro-electrode, Mater. Des. 193 (2020) 108812.

[24] J.D. Arregui-Mena, R.N. Worth, W. Bodel, B. März, W. Li, A.A. Campbell, E. Cakmak, N. Gallego, C. Contescu, P.D. Edmondson, Multiscale characterization and comparison of historical and modern nuclear graphite grades, Mater. Charact. 190 (2022) 112047.

[25] J.D. Arregui-Mena, D. Griffiths, R.N. Worth, C.E. Torrence, A. Selby, C. Contescu, N. Gallego, P.D. Edmondson, P.M. Mummery, L. Margetts, Using porous random fields to predict the elastic modulus of unoxidized and oxidized superfine graphite, Mater. Des. 220 (2022) 110840.

[26] M. Dowell, R. Howard, Tensile and compressive properties of flexible graphite foils, Carbon 24 (1986) 311–323.

[27] J. Gu, Y. Leng, Y. Gao, H. Liu, F. Kang, W. Shen, Fracture mechanism of flexible graphite sheets, Carbon 40 (2002) 2169–2176, https://doi.org/10.1016/S0008-6223(02)00075-1.

[28] M. Cermak, M. Bahrami, Compression behavior of natural graphite sheet, SN Appl. Sci. 2 (2020) 1–7.

[29] F. Martoïa, L. Orgéas, P.J. Dumont, J.F. Bloch, F. Flin, J. Viguié, Crumpled paper sheets: low-cost biobased cellular materials for structural applications, Mater. Des. 136 (2017) 150–164, https://doi.org/10.1016/j.matdes.2017.09.031.

[30] O. Bouaziz, J.P. Masse, S. Allain, L. Orgéas, P. Latil, Compression of crumpled aluminum thin foils and comparison with other cellular materials, Mater. Sci. Eng. A 570 (2013) 1–7, https://doi.org/10.1016/j.msea.2013.01.031.

[31] S. Cottrino, P. Viviès, D. Fabrègue, E. Maire, Mechanical properties of crumpled aluminum foils, Acta Mater. 81 (2014) 98–110, https://doi.org/10.1016/j.actamat.2014.07.069.

[32] J.A. Baimova, E.A. Korznikova, S.V. Dmitriev, B. Liu, K. Zhou, Review on crumpled graphene: unique mechanical properties, Rev. Adv. Mater. Sci. 39 (2014) 69–83.

[33] Y. Liao, Z. Li, W. Xia, et al., Size-dependent structural behaviors of crumpled graphene sheets, Carbon 174 (2021) 148–157.

[34] A.B. Croll, T. Twohig, T. Elder, The compressive strength of crumpled matter, Nat. Commun. 10 (2019) 1502.

[35] G. Giménez-Ribes, E. van der Linden, M. Habibi, Auxetic behavior and unusual shear resistance of crumpled materials: opportunities for programming the nonlinear responses of crumpled mechanical metamaterials, Mater. Des. 223 (2022) 111258.

[36] O. Bouaziz, R. Bouafif, R. Massion, Sandwich materials with a crumpled aluminium core, Metall. Res. Technol. 118 (2021) 320.

[37] M. Ganjian, S. Janbaz, T. van Manen, N. Tümer, K. Modaresifar, M. Minneboo, L.E. Fratila-Apachitei, A.A. Zadpoor, Controlled metal crumpling as an alternative to folding for the fabrication of nanopatterned meta-biomaterials, Mater. Des. 220 (2022) 110844.
[38] A.K. Piñón-Vázquez, S.M.V. Díaz, D. Meneses-Rodríguez, L.A. Alcaraz-Caracheo, F. Tristán, Self-standing tridimensional structures from crumpling techniques made with composite films of polylactic acid and exfoliated graphite, Mater. Des. (2023) 112102.
[39] E. Solfiti, F. Berto, Mechanical properties of flexible graphite, Procedia Strucy. Integr. 25 (2020) 420–429.
[40] A.V. Ivanov, N.V. Maksimova, M.S. Manylov, A.N. Kirichenko, I.L. Kalachev, A.P. Malakho, V.V. Avdeev, Gas permeability of graphite foil prepared from exfoliated graphite with different microstructures, J. Mater. Sci. 56 (2021) 4197–4211.
[41] A. Celzard, J. Mareche, G. Furdin, Modelling of exfoliated graphite, Prog. Mater. Sci. 50 (2005) 93–179.
[42] M. Inagaki, T. Suwa, Pore structure analysis of exfoliated graphite using image processing of scanning electron micrographs, Carbon 39 (2001) 915–920.
[43] P.-H. Chen, D. Chung, Elastomeric behavior of exfoliated graphite, as shown by instrumented indentation testing, Carbon 81 (2015) 505–513.
[44] Y. Leng, J. Gu, W. Cao, T.-Y. Zhang, Influences of density and flake size on the mechanical properties of flexible graphite, Carbon 36 (1998) 875–881.
[45] A. Yoshida, Y. Hishiyama, M. Inagaki, Exfoliated graphite from various intercalation compounds, Carbon 29 (1991) 1227–1231.
[46] L. Xiao, D. Chung, Mechanical energy dissipation modeling of exfoliated graphite based on interfacial friction theory, Carbon 108 (2016) 291–302.
[47] A. Celzard, J. Marêché, G. Furdin, Describing the properties of compressed expanded graphite through power laws, J. Phys. Condens. Matter 15 (2003) 7213.
[48] P.H. Chen, D.D. Chung, Viscoelastic behavior of the cell wall of exfoliated graphite, Carbon 61 (2013) 305–312, https://doi.org/10.1016/j.carbon.2013.05.009.
[49] H. Toda, K. Tsubone, K. Shimizu, K. Uesugi, A. Takeuchi, Y. Suzuki, M. Nakazawa, Y. Aoki, M. Kobayashi, Compression and recovery micro-mechanisms in flexible graphite, Carbon 59 (2013) 184–191, https://doi.org/10.1016/j.carbon.2013.03.008.
[50] M. Kobayashi, H. Toda, A. Takeuchi, K. Uesugi, Y. Suzuki, Three-dimensional evaluation of the compression and recovery behavior in a flexible graphite sheet by synchrotron radiation microtomography, Mater. Charact. 69 (2012) 52–62, https://doi.org/10.1016/j.matchar.2012.04.008.
[51] X.H. Wei, L. Liu, J.X. Zhang, J.L. Shi, Q.G. Guo, Mechanical, electrical, thermal performances and structure characteristics of flexible graphite sheets, J. Mater. Sci. 45 (2010) 2449–2455, https://doi.org/10.1007/s10853-010-4216-y.
[52] E.A. Efimova, D.A. Syrtsova, V.V. Teplyakov, Gas permeability through graphite foil: the influence of physical density, membrane orientation and temperature, Sep. Purif. Technol. 179 (2017) 467–474, https://doi.org/10.1016/j.seppur.2017.02.023.
[53] M. Krzesińska, A. Celzard, J.F. Marêché, S. Puricelli, Elastic properties of anisotropic monolithic samples of compressed expanded graphite studied with ultrasounds, J. Mater. Res. 16 (2001) 606–614, https://doi.org/10.1557/JMR.2001.0087.
[54] H.O. Pierson, Handbook of Carbon, Graphite, Diamonds and Fullerenes: Processing, Properties and Applications, William Andrew, 2012.
[55] E. Solfiti, F. Berto, A review on thermophysical properties of flexible graphite, Procedia Strucy. Integr. 26 (2020) 187–198.
[56] E. Solfiti, M. Calviani, A. Perillo-Marcone, J.M. Heredia, C. Torregrosa, A. Alvaro, F. Berto, Flexible graphite as beam dumping material in the TDE blocks of the large hadron collider, Procedia Strucy. Integr. 28 (2020) 2228–2234, https://doi.org/10.1016/j.prostr.2020.11.051.
[57] E.P. Randviir, D.A. Brownson, C.E. Banks, A decade of graphene research: production, applications and outlook, Mater. Today 17 (2014) 426–432.
[58] ASTM D695-15 Standard Test Method for Compressive Properties of Rigid Plastics, https://doi.org/10.1520/D0695-15.2, 2015, 1–8.
[59] I. ISO, Mechanical Testing of Metals—Ductility Testing—Compression Test for Porous and Cellular Metals, 2011, Google Scholar, 2011.
[60] Y. Sun, B. Amirrasouli, S.B. Razavi, Q. Li, T. Lowe, P. Withers, The variation in elastic modulus throughout the compression of foam materials, Acta Mater. 110 (2016) 161–174.
[61] M. Bonnissel, L. Luo, D. Tondeur, Compacted exfoliated natural graphite as heat conduction medium, Carbon 39 (2001) 2151–2161, https://doi.org/10.1016/S0008-6223(01)00032-X.
[62] I.M. Afanasov, D.V. Savchenko, S.G. Ionov, D.A. Rusakov, A.N. Seleznev, V.V. Avdeev, Thermal conductivity and mechanical properties of expanded graphite, Inorg. Mater. 45 (2009) 486–490, https://doi.org/10.1134/S0020168509050057.
[63] M. Pollock, GRAFOIL - Flexible Graphite - Engineering Design Manual, 2nd edition, 2002.
[64] I. Gibson, M.F. Ashby, The mechanics of three-dimensional cellular materials, Proc. R. Soc. Lond. Ser. A, Math. Phys. Sci. 382 (1982) 43–59.
[65] O. Blakslee, D. Proctor, E. Seldin, G. Spence, T. Weng, Elastic constants of compression-annealed pyrolytic graphite, J. Appl. Phys. 41 (1970) 3373–3382.
[66] W.H. Smith, D.H. Leeds, Pyrolytic graphite, Mod. Mater. 7 (1970) 139–221.
[67] F. Balima, S. Le Floch, A. San-Miguel, P. Lindner, A. Brûlet, L. Duclaux, V. Pischedda, Shear effects on expanded graphite under uniaxial pressure: an in situ small angle neutron scattering study, Carbon 74 (2014) 54–62, https://doi.org/10.1016/j.carbon.2014.03.002.
[68] J. Luo, H.D. Jang, T. Sun, L. Xiao, Z. He, A.P. Katsoulidis, M.G. Kanatzidis, J.M. Gibson, J. Huang, Compression and aggregation-resistant particles of crumpled soft sheets, ACS nano 5 (2011) 8943–8949.
[69] A.D. Cambou, N. Menon, Three-dimensional structure of a sheet crumpled into a ball, Proc. Natl. Acad. Sci. USA 108 (2011) 14741–14745, https://doi.org/10.1073/pnas.1019192108.
[70] T. Tallinen, J. Åström, J. Timonen, The effect of plasticity in crumpling of thin sheets, Nat. Mater. 8 (2009) 25–29.
[71] S.W. Cranford, M.J. Buehler, Packing efficiency and accessible surface area of crumpled graphene, Phys. Rev. B 84 (2011) 205451.
[72] J. Andrejevic, L.M. Lee, S.M. Rubinstein, C.H. Rycroft, A model for the fragmentation kinetics of crumpled thin sheets, Nat. Commun. 12 (2021) 1470.
[73] Q. Tan, P. Liu, C. Du, L. Wu, G. He, Mechanical behaviors of quasi-ordered entangled aluminum alloy wire material, Mater. Sci. Eng. A 527 (2009) 38–44.
[74] P. Liu, Q. Tan, L. Wu, G. He, Compressive and pseudo-elastic hysteresis behavior of entangled titanium wire materials, Mater. Sci. Eng. A 527 (2010) 3301–3309, https://doi.org/10.1016/j.msea.2010.02.071.
[75] D. Hughes, E.H. Amalu, T. Pak, R. Kennedy, Effect of relative density on compressive load response of crumpled aluminium foil mesh, Materials 12 (2019), https://doi.org/10.3390/ma12234018.
[76] E.J. Seldin, Stress-strain properties of polycrystalline graphites in tension and compression at room temperature, Carbon 4 (1966) 177–191, https://doi.org/10.1016/0008-6223(66)90079-0.
[77] M.W. Barsoum, A. Murugaiah, S.R. Kalidindi, T. Zhen, Y. Gogotsi, Kink bands, nonlinear elasticity and nanoindentations in graphite, Carbon 42 (2004) 1435–1445, https://doi.org/10.1016/j.carbon.2003.12.090.
[78] R.A. Guyer, P.A. Johnson, Nonlinear mesoscopic elasticity: evidence for a new class of materials, Phys. Today 52 (1999) 30–36, https://doi.org/10.1063/1.882648.
[79] G.M. Jenkins, Analysis of the stress-strain relationships in reactor grade graphite, Br. J. Appl. Phys. 13 (1962) 30–32, https://doi.org/10.1088/0508-3443/13/1/307.